

Article | Received 6 January 2025; Accepted 18 March 2025; Published 18 April 2025
<https://doi.org/10.55092/sc20250006>

Predicting bond-slip behaviour in grouted bellows connect rebar using deep learning

Yihu Chen^{1,2}, Xingshuo Yang¹, Jingchao Lin¹, Guangxin Xie¹, Min Zhang^{1,*} and Yanwei Wang^{1,*}

¹ Guangxi Key Laboratory of Green Building Materials and Construction Industrialization, Guilin University of Technology, Guilin 541004, China

² School of Architecture and Electrical Engineering, Hezhou University, Hezhou 542899, China

* Correspondence authors; E-mails: 2000022@glut.edu.cn; wangyanwei@glut.edu.cn.

Highlights:

- A deep learning network is proposed to predict the bond slip performance of GBR systems.
- Deep learning models have better prediction accuracy than empirical formulas.
- An improved hyperbolic constitutive model based on deep learning is proposed.
- The constitutive model is applied to the numerical simulation of ABAQUS with good results.

Abstract: Grouted Bellows Connect Rebar (GBR) technology is critical for ensuring reliable connections in precast concrete components. The bond-slip behaviour, a core metric for assessing GBR connection performance, presents significant complexity, and existing empirical models often fall short in prediction accuracy to meet engineering demands. Addressing this challenge, this study introduces an innovative hybrid model (CNN-LSTM) that integrates convolutional neural networks with long short-term memory networks. Utilizing eight critical parameters, such as grouting strength, reinforcement ultimate strength, and the anchorage length-to-diameter ratio of the reinforcement, the model achieves precise predictions of GBR bond stress. This study systematically collected data from 114 sets of GBR pull-out tests, constructing a dataset comprising 2,272 bond-slip samples for model training and validation. Additionally, 15 GBR independent samples were independently fabricated and multiple samples were extracted to assess the model generalization capability. Experimental results demonstrate that the CNN-LSTM model significantly outperforms traditional empirical models in predicting bond stress and exhibits superior generalization across key metrics, including total energy consumption, maximum bond stress, failure modulus, and residual energy. Parameter importance analysis reveals that grouting strength, reinforcement ultimate strength, and the anchorage length-to-diameter ratio are the most influential factors in bond stress prediction. Building on the CNN-LSTM model predictions, this study establishes an improved empirical model with clear physical significance, offering a reliable computational foundation for engineering applications.

Keywords: grouting bellows; precast concrete components; CNN-LSTM; bond stress; energy consumption; maximum bond stress



Copyright©2025 by the authors. Published by ELSP. This work is licensed under Creative Commons Attribution 4.0 International License, which permits unrestricted use, distribution, and reproduction in any medium provided the original work is properly cited.

1. Introduction

With the increasing demand for joint anchorage in the construction of prefabricated structures, the issue of bond-slip between reinforcement and grouting material has garnered significant attention from researchers [1]. Sleeve grouting connection [2] and GBR are two prevalent connection methods in prefabricated concrete buildings. However, the former requires high construction accuracy, leading to reduced construction efficiency, whereas the bellows grouting anchor connection has lower accuracy requirements [3]. Research by Li [4] further demonstrates that in GBR systems, metal bellows exhibit superior anchoring performance compared to plastic bellows. Additionally, multiple pull-out tests have verified the reliability of UHPC grouting material in fabricated joint connection technology. GBR system represents a critical technology for ensuring the reliable connection of precast concrete components.

The GBR system, designed for connecting prefabricated piers and cap beams, was first introduced by Steuck *et al.* [5]. Steuck pull-out tests indicate that reductions in grouting strength and anchoring length lead to the deterioration of the anchoring performance of steel bars, thereby affecting the stability and integrity of the overall structure. In the joint design of prefabricated concrete buildings, the anchoring performance in the GBR system is primarily determined by the bond-slip relationship between steel bars and grout, which has garnered extensive attention in relevant studies [6]. To investigate the main factors influencing the bond-slip behavior between reinforcement and grout, Hayashi *et al.* [7] and Yu *et al.* [8] explored the complex variations in bond strength by altering parameters such as the diameter of reinforcement, anchorage length, grout strength, and protective layer thickness, in addition to conducting tensile tests. Beyond tensile tests, Hosseini *et al.* [9,10] and Gu *et al.* [11] examined the bond-slip mechanism of steel bars in axial pull-out processes through beam tests to achieve a more accurate understanding of the anchorage mechanical properties between steel bars and grout. Hosseini *et al.* [9,10] utilized spiral constraints to study the bond-slip relationship of threaded steel bars connected by grout, finding that factors such as spiral diameter and spiral spacing impact the restraint effect of the system. Gu's beam tests revealed that the anchorage performance of precast grout members significantly exceeds that of cast-in-place concrete structures. Zhao *et al.* [12] investigated the performance of bellow slurry anchor connections under spiral stirrup constraints and proposed formulas for ultimate bond strength and ultimate anchoring length, demonstrating that ultimate bond strength changes nonlinearly with increasing bellows diameter. Although prior studies have identified critical factors influencing GBR anchoring performance, the precise bond stress-slip relationship between reinforcement and grout remains underexplored.

To simulate the finite element analysis of large assembled components under various loads, the bond-slip model between reinforcement and grout serves as a crucial foundation [13,14]. In the GBR system, the force mechanism at the contact interface between the steel bar and the grout is highly complex. In addition to the mechanical interlock provided by the transverse ribs of the steel bar, the gripping force exerted by the metal bellows helps mitigate the spread of cracks in the grout [15]. Through extensive central pull-out tests, displacement and load data from the loading end of the GBR system can be directly obtained, allowing for the calculation of the bond-slip relationship. Subsequently, statistical and fitting methods can be employed to propose a bond-slip model for the GBR system. Liu [16], based on data fitting from pull-out tests of grouted metal bellows, provided a simplified bond-slip model that considers critical factors such as reinforcement anchorage length and aperture ratio. Zhu [17] established

a bond-slip model between grout and reinforcement under spiral stirrup constraints, based on the characteristics of the bond-slip curve. In addition to the slip between steel bars and grout, the GBR system also exhibits slip between the bellows and external concrete, rendering the bond-slip properties of the structure highly complex. The aforementioned models only consider a limited set of variables and fail to account for more critical factors, such as the maximum distance between the steel bar and the edge of the member. By collecting extensive research data and extracting several key factors as input features, machine learning methods can be employed to solve the bond-slip model between reinforcement and grout in the GBR system.

In the study of applying machine learning to bond-slip models, Abdulwarith *et al.* [18] employed particle swarm optimization artificial neural networks and support vector machine models to investigate the bond-slip behavior between UHPC and steel bars, exploring the complex relationships among steel bar yield strength, concrete cover thickness, and other factors affecting ultimate bond strength. Fan *et al.* [19] effectively predicted the bond-slip relationship between steel and concrete using radio frequency feature selection and GWO-SVR. Su *et al.* [20] utilized MLR, SVM, and ANN models to predict the bond strength between FRP bars and concrete, and developed a stacking strategy to enhance prediction accuracy. To accurately predict the local bond-slip relationship at the interface between steel bars and UHPC under monotonic load, particularly in the absence of sufficient data, Pishro *et al.* [21] created a database using finite element analysis and employed a physical information neural network (PINN) to predict hyperparameters in the bond-slip problem between steel bars and UHPC. This approach provides an effective optimization scheme for structural engineering. It is noteworthy that the bond-slip model of the GBR system can be viewed as a nonlinear curve closely related to time, making it suitable for training using multivariate temporal networks as time series data [22,23].

Due to the complexity of bond-slip behavior in GBR systems and the limited research on integrating bond-slip models with machine learning for GBR systems, this paper proposes a deep learning network for time series data processing to address this issue and thoroughly analyze the bond-slip constitutive behavior in GBR systems. In this study, a substantial amount of pull-out test data from GBR systems was collected, and a deep learning model based on time series analysis was developed to predict the bond-slip relationship between reinforcement and grout in GBR systems. Additionally, 15 groups of pull-out tests were conducted to validate the predictive accuracy of the model. Furthermore, the deep learning model with the best predictive performance was compared with traditional constitutive model, and an in-depth analysis was conducted on total energy consumption, maximum bond strength, component failure modulus, and residual energy. The study also provides an importance analysis of the influencing factors of GBR on total energy consumption and other indicators. Although the CNN-LSTM model demonstrates high precision in predictive capabilities, its internal mechanisms are complex and cannot be easily expressed through simple mathematical formulas. To facilitate the quick evaluation of GBR systems, a simplified bond-slip model is proposed. This model is based on the ultimate bond stress predicted by the CNN-LSTM model and incorporates a modified hyperbolic bond-slip model for engineer reference. The aim of this study is to offer an effective method for researchers and structural engineers to understand and design the bond-slip relationship between steel bars and grout in GBR systems, thereby enhancing the reliability of joint design in prefabricated buildings.

2. Database and experiment

2.1. Database

This section provides an overview of the collected database, key component factors for GBR systems, and the inputs and outputs of the deep learning model. The database is derived from 11 studies on GBR, encompassing 114 components tested under normal temperature and pressure conditions. Data points from the bond stress-slip curves corresponding to each component were extracted, resulting in a database with 2272 training data points. The components in the database consist of a single steel bar anchored in a corrugated tube within the grouting material, subjected to unidirectional axial pull-out tests. These components were fabricated in accordance with the design specifications of ACI318-19 [24] or GB50010-2010 [25]. The failure mode observed in these components is adhesive slip failure, characterized by the steel bars slipping out of the high-strength grout material due to anchorage failure. For the input parameters of the deep learning model, the following variables were selected: f_c' , f_g' , l_r/d_r , d_b/d_r , D_r , f_u , f_y and s . Their significance and the scope of the database are presented in Table 1, while the detailed range of each input parameter in each study is shown in Table 2. These parameters were chosen for the following reasons:

The ratio of reinforcement anchorage length to reinforcement diameter (l_r/d_r) and the ratio of inner diameter of bellows to reinforcement diameter (d_b/d_r) are critical factors. During the reinforcement pull-out process, the stress distribution is uneven from the loading end to the anchoring end. The stress distribution function equation has been studied using normalization methods [26, 27]. The ultimate bond-slip strength is proportional to the anchorage length of the steel bar, and the likelihood of steel bar pull-out failure increases with the anchorage length [25, 28]. When the aperture of the metal bellows embedded in concrete is too small relative to the steel bar, insufficient grouting material may lead to the bellows being pulled out along with the steel bar due to local effects. The aperture ratio thus has a significant impact on bond-slip performance [29]. Therefore, these factors are crucial to the anchoring performance of GBR systems.

The tensile strength (f_u) and yield strength (f_y) of the steel bar are critical material properties that play a decisive role in the anchoring capability of the GBR system.

Concrete compressive strength (f_c') and grouting splitting tensile strength (f_g') are critical parameters as the grouting material is in direct contact with the reinforcement. The anchoring effect in the GBR system is primarily provided by the mechanical interlock between the ribbed reinforcement and the grouting material. When the load is sufficiently large, the transverse ribs of the reinforcement bar can crush the grouting material, leading to micro-cracks and ultimately causing cracking and failure of the grouting material [30–32]. During the pull-out process, the corrugated pipe exerts a gripping force on the steel bar, which increases the friction between the steel bar and the grout material, thereby enhancing the bond properties. However, when the expansion and deformation of the bellows induce cracks in the surrounding concrete, the gripping force of the bellows is also diminished [33].

Minimum distance between the reinforcement bar and the edge of the member (D_r): A concrete cover that is too thin can lead to premature cracking during the loading process. This premature cracking weakens the binding effect of the concrete on the bellows, thereby adversely affecting the bond-slip relationship in the GBR system [34,35].

Slip increments (s) are input and trained in the bond-slip curve as the horizontal axis. Each slip increment corresponds to a bond stress, so the bond stress output after model training will also correspond to

these slip increments, thereby directly obtaining the bond-slip model relationship. A detailed example of each parameter for a component is shown in Figure 1.

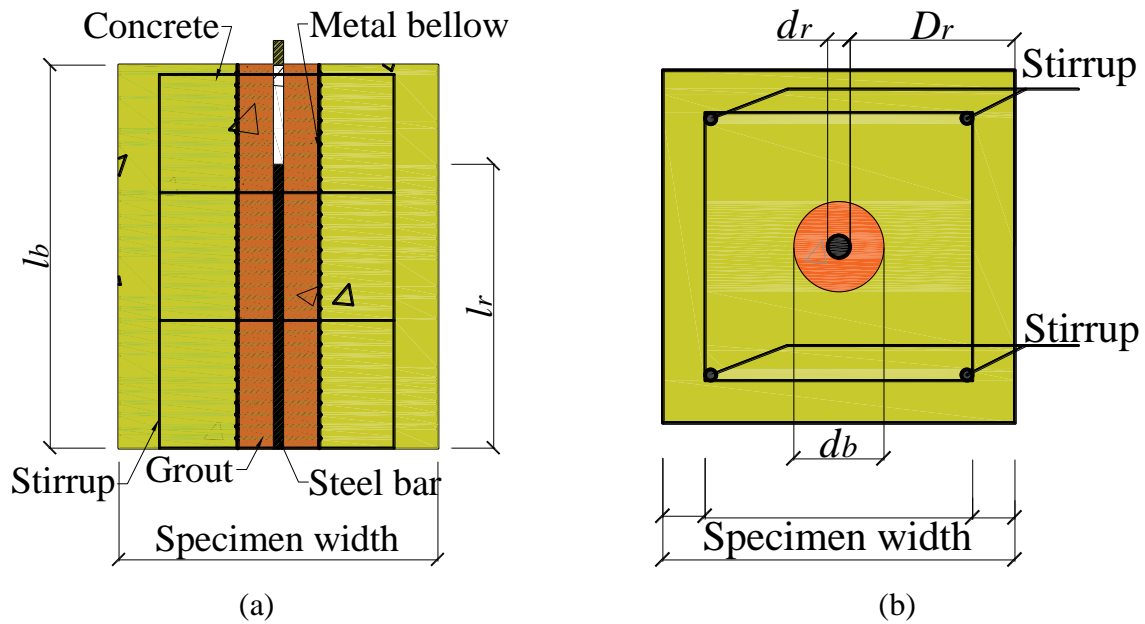


Figure 1. Schematic diagram of input parameters and specimen geometry (a) Vertical section view; (b) Horizontal section view.

Table 1. Input parameter meaning and range.

Input parameter	Meaning	Range
f_c' (MPa)	Concrete compressive strength	34.5-45.89 MPa
f_g' (MPa)	Tensile strength of grout	3.74-6.82 MPa
l_r / d_r	Ratio of anchorage length to diameter of reinforcement bar	1.96-23.5
d_b / d_r	Ratio of the diameter of the bellows to the diameter of the steel bar	1.44-4.94
D_r (mm)	Minimum distance between steel bar and member edge	30-457.2 mm
f_u (MPa)	Ultimate strength of steel bar	566.5-925 MPa
f_y (MPa)	Yield strength of steel bar	422-580 MPa
s (mm)	Slip of the loading end of the bar	0-96.1 mm

Table 2. Detailed scope of component parameters.

Source	f_c' (MPa)	f_g' (MPa)	l_r / d_r	d_b / d_r	D_r (mm)	f_u (MPa)	f_y (MPa)	s (mm)
Guo ^[36]	45.89	[3.83, 4.25]	[5, 13]	[1.6, 3.6]	[130, 190]	645.3	452.6	[0, 22]
He ^[37]	45.17	4.13	[4, 7]	[8, 11]	[55, 85]	[581, 604.4]	[444.8, 458]	[0, 18.8]
Pan ^[38]	45.17	4.13	[5, 10]	[1.44, 4.38]	[30, 315]	[579, 665]	[435, 529.5]	[0, 15.8]
Liu ^[39]	34.7	3.74	[7, 13]	4.29	30	[566.5, 603]	[431, 495.5]	[0, 18.6]
Chen ^[40]	43.1	3.93	[5.04, 7.2]	[1.44, 2]	[175, 375]	591.7	451.2	[0, 96.1]
Guo ^[41]	45.89	[3.83, 4.25]	[5, 16]	2.6	[125, 375]	647.3	452.6	[0, 23.03]

Table 2. Cont.

Source	f_c' (MPa)	f_g' (MPa)	l_r / d_r	d_b / d_r	D_r (mm)	f_u (MPa)	f_y (MPa)	s (mm)
Zhu ^[42]	39.5	[5.09, 6.82]	[3, 5]	[2.5, 4.29]	75	[568.2, 599]	[433, 445.4]	[0, 28.05]
Zhou ^[43]	44.8	4.74	[1.96, 23.46]	[2.23, 4.33]	120	[726.7, 925]	[511, 580]	[0, 79.74]
Hu ^[44]	42.3	5.79	7	2.52	250	601	422	[0, 57.28]
Liu ^[45]	42.3	5.31	[3, 5]	[2.52, 4.94]	125	[603, 610]	[422, 437]	[0, 13.77]
Steuck ^[5]	34.47	4.94	[4, 14]	[3.4, 3.44]	457.2	648	[455, 510]	[0, 27.71]

2.2. Experiment

Following the central pull test of the database, we independently prepared 15 sets of tests to verify the robustness of the model. The detailed drawing of the bar bond-slip specimen is shown in Figure 1. The test employs a mono-continuous loading mode, with the schematic diagram of the loading device illustrated in Figure 2. The steel bar is anchored using an anchor rod, and the drawing force is evenly transferred to the anchor rod via a steel plate. The load is applied at a rate of 10 kN/min during the initial stage, and subsequently reduced to 5 kN/min when the steel bar load reaches 85% of the estimated ultimate load, continuing until the steel bar fails.

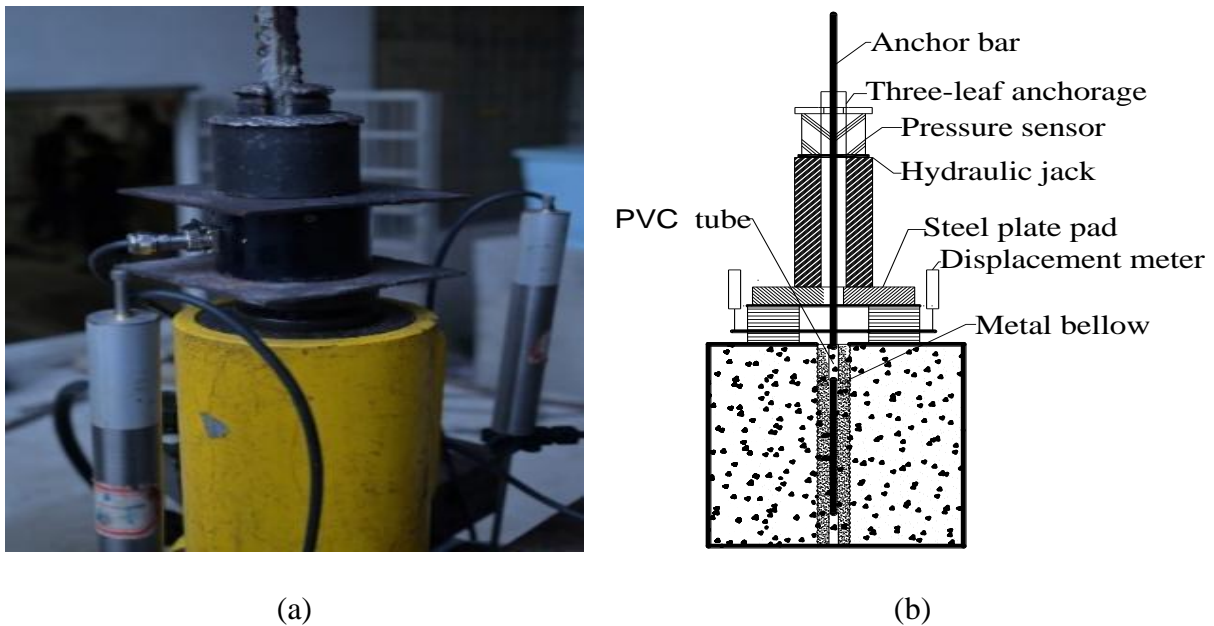


Figure 2. Loading set up (a) Loading device; (b) Loading device design drawing.

3. Model development

3.1. CNN-LSTM model

The model is determined based on the characteristics of the input and output parameters. Among the input values, the tensile strength of the steel bar, the yield strength of the steel bar, the compressive strength of the

concrete, and the grouting splitting tensile strength are the material parameters of the specimen. The ratio of anchorage length to the diameter of the steel bar, the ratio of the inner diameter of the bellows to the diameter of the steel bar, and the minimum distance between the steel bar and the edge of the member are the geometric parameters of the specimen. The slip quantity represents the time series data that changes over the course of the test, while the output value is the bond stress, which is also time series data. When designing the model, it is essential to extract local features from the time series data while maintaining the original sequence relationship. Therefore, a CNN-LSTM architecture is proposed. CNNs can efficiently extract local features of the data and have translation invariance, while LSTM can capture long-term dependencies in the data [46]. The model architecture of CNN-LSTM is shown in Figure 3. During the training process, data is first input into the convolutional layer where features are extracted using convolutional kernels. The flat layer is used to reduce the feature dimensions before inputting them into the LSTM layer. Finally, a Sigmoid activation function is employed to obtain the predicted values, and the Adam algorithm is used to calculate the gradient of each layer for backpropagation.

Training with larger batch sizes significantly improved the CNN-LSTM model accuracy. Therefore, 256 was adopted as the batch size for the data of 2272. Specifically, a dataset comprising 2272 entries was sequentially arranged and divided into batches of 1000 for input into the convolutional layer. The convolutional layers comprised 64 filters with a stride length of 1. The data undergoes folding operations, generating weight and bias tensors. Following the application of the ReLu activation function for non-linear processing, the data proceeds to the subsequent convolutional layer, also composed of 64 layers, where it is again folded with a stride length of 1 to generate additional weights and biases. The processed data is then transformed into a one-dimensional time series through flattening layers and subsequently input into the LSTM network for training. The final output is a bond stress vector, derived from the fully connected layer. The network undergoes backpropagation using the objective function, as illustrated in Equation (1). This process encapsulates the learning mechanism of the CNN-LSTM model.

$$L = \sqrt{\frac{1}{N} \sum_{i=1}^N (y_i - \hat{y}_i)^2} \quad (1)$$

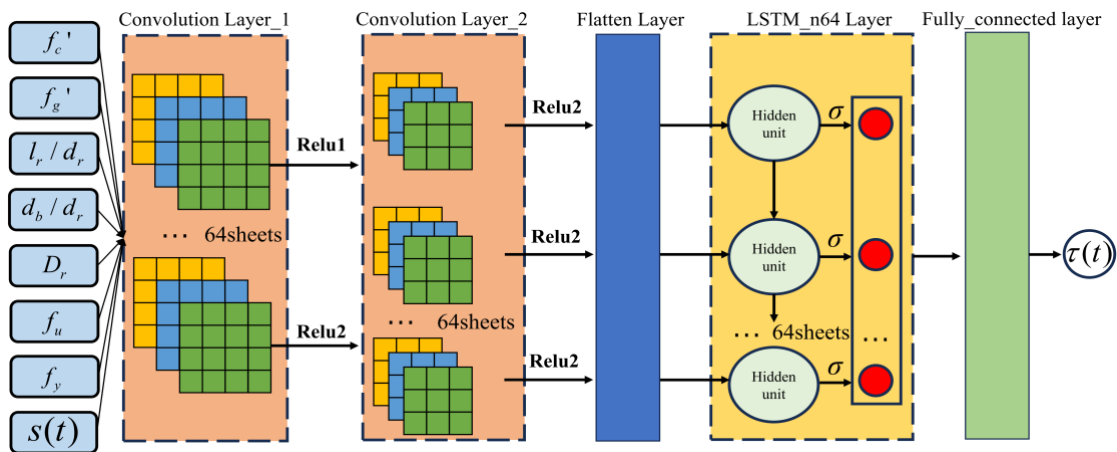


Figure 3. CNN-LSTM.

3.2. Data preprocessing and hyper-parameter setting

Before model training, all data in the database must be normalized to ensure that no single feature disproportionately influences the results. The values are normalized to fall within the range of 0 to 1. The normalization formula is as follows:

$$\mathbf{x}_{i,new} = \frac{|\mathbf{x}_i - \mathbf{x}_{\max}|}{|\mathbf{x}_{\max} - \mathbf{x}_{\min}|} \quad (2)$$

After normalizing the dataset, the data were randomly divided into five parts for hyperparameter selection using the five-fold cross-validation method. The mini-batch size was determined to be 256, the number of epochs was set to 100, the initial learning rate was 0.001. The hyperparameters were configured using the options function. All models in this study were trained on a system equipped with an Intel i7-12650H CPU, operating at up to 4.7 GHz, and an RTX 4060 GPU, featuring 3072 CUDA cores and 8 GB of GDDR6 memory. Drawing from extensive deep learning experience and the breadth of available databases, it is established that the optimal configuration for all temporal networks consists of 1 or 2 hidden layers, with each layer comprising 32 or 64 units. Consequently, it is necessary to individually assess the performance of each model under varying numbers of hidden layer units. For CNN-LSTM, two configurations are considered: one with two hidden layers, each containing 32 units, and another with a single hidden layer comprising 64 units.

To evaluate CNN-LSTM and identify the hidden layer and unit configuration with the highest prediction accuracy, four commonly used machine learning regression metrics are employed: coefficient of determination (R^2), root mean square error (RMSE), mean absolute error (MAE), and mean absolute percentage error (MAPE). These metrics assess the model prediction accuracy and generalization capability. R^2 value approaching 1 indicates superior model fitting, while RMSE and MAE values closer to 0 signify minimal fitting error. MAPE value of 0% denotes perfect model prediction, whereas values exceeding 100% indicate poor model performance. The formulas for these four metrics are provided in equations (3) to (6).

$$R^2 = \frac{\sum_{i=1}^N \left(\hat{y}_i - \bar{y} \right)^2}{\sum_{i=1}^N \left(y_i - \bar{y} \right)^2} \quad (3)$$

$$RMSE = \sqrt{\frac{\sum_{i=1}^N \left(y_i - \hat{y}_i \right)^2}{N}} \quad (4)$$

$$MAE = \frac{\sum_{i=1}^N \left| \tau_i - \hat{\tau}_i \right|}{N} \quad (5)$$

$$MAPE = \left(\frac{100\%}{n} \right) \sum_{i=1}^N \left| y_i - \hat{y}_i \right| / y_i \quad (6)$$

The performance indicators for CNN-LSTM_n32h2 and CNN-LSTM_n64, as evaluated on both the training and test sets, are presented in Table 3. Both horizontal and vertical comparative analyses reveal that CNN-LSTM_n64 demonstrates superior prediction accuracy.

Table 3. Hyperparameter evaluation.

Model	R ² of Training set	RMSE of Training set	MAE of Training set	MAPE of Training set	R ² of Test set	RMSE of Test set	MAE of Test set	MAPE of Test set
CNN-LSTM_n32h2	0.954	6.112	3.48	19.57%	0.911	11.021	5.11	29.01%
CNN-LSTM_n64	0.962	5.589	2.64	16.7%	0.926	10.238	4.87	28%

4. Results

4.1. Comparison with empirical model

In the study of GBR systems, several researchers have conducted numerous unidirectional pull-out tests and fitted the test data to derive the bond-slip model [8, 47–49]. Because there are few researches on the bond slip constitutive of GBR system, and few of them conform to the feasibility of prediction. This paper selects the study by LIU [45] to compare the prediction results of the bond-slip model obtained through GBR system data statistics with those of the time series analysis model. The objective is to verify that the deep learning model offers higher prediction accuracy than the empirical formulas derived from experiments, thereby saving significant material and labour resources. Based on the theoretical formula derived from the physical equation containing the position function calculated by scholars, Liu fitted the model between bond stress and slip amount using data from central pull-out experiments on 15 groups of reference specimens, as shown in equations (7–11) where τ_u is the ultimate bond stress, τ_r is the residual bond stress, s_r and s_u represent the residual slippage and ultimate slippage, respectively.

$$\tau(s) = \begin{cases} \tau_u (2.02s^{1.51}) / (1 + 2.02s^{1.51}), & s < s_u \\ \tau_u - (\tau_u - \tau_r) / (s_r - s_u), & s_u \leq s \leq s_r \\ 0.6\tau_u, & s > s_r \end{cases} \quad (7)$$

$$\tau_u = (0.9 + 0.43 \frac{d_r}{l_r}) [1.29 + 1.92 \frac{d_b}{d_r} - 0.29 (\frac{d_b}{d_r})^2] f'_g \quad (8)$$

$$\tau_r = 0.6\tau_u \quad (9)$$

$$s_r = (1.03 - 0.19 \frac{d_r}{l_r}) [1.43 + 1.48 \exp(-0.84 \frac{d_b}{d_r})] f'_g \quad (10)$$

The CNN-LSTM model and the bond-slip model proposed by Liu were used to predict and analyze the results of Liu experiment. The outcomes are presented in Figure 4, with the numerical values in the figure corresponding to those in Liu paper. The CNN-LSTM model accurately predicted the bond-slip behaviour observed in Liu's experiments, achieving an R² of 0.926 on the test set. As shown in Figure 4(g)–(o), the empirical model fitting is less accurate compared to CNN-LSTM. The ultimate bond stress predicted by the empirical model deviates more significantly from the test results, whereas CNN-LSTM aligns more closely with the experimental data across all results. These findings demonstrate that CNN-LSTM exhibits superior predictive accuracy and generalization performance compared to the empirical model.

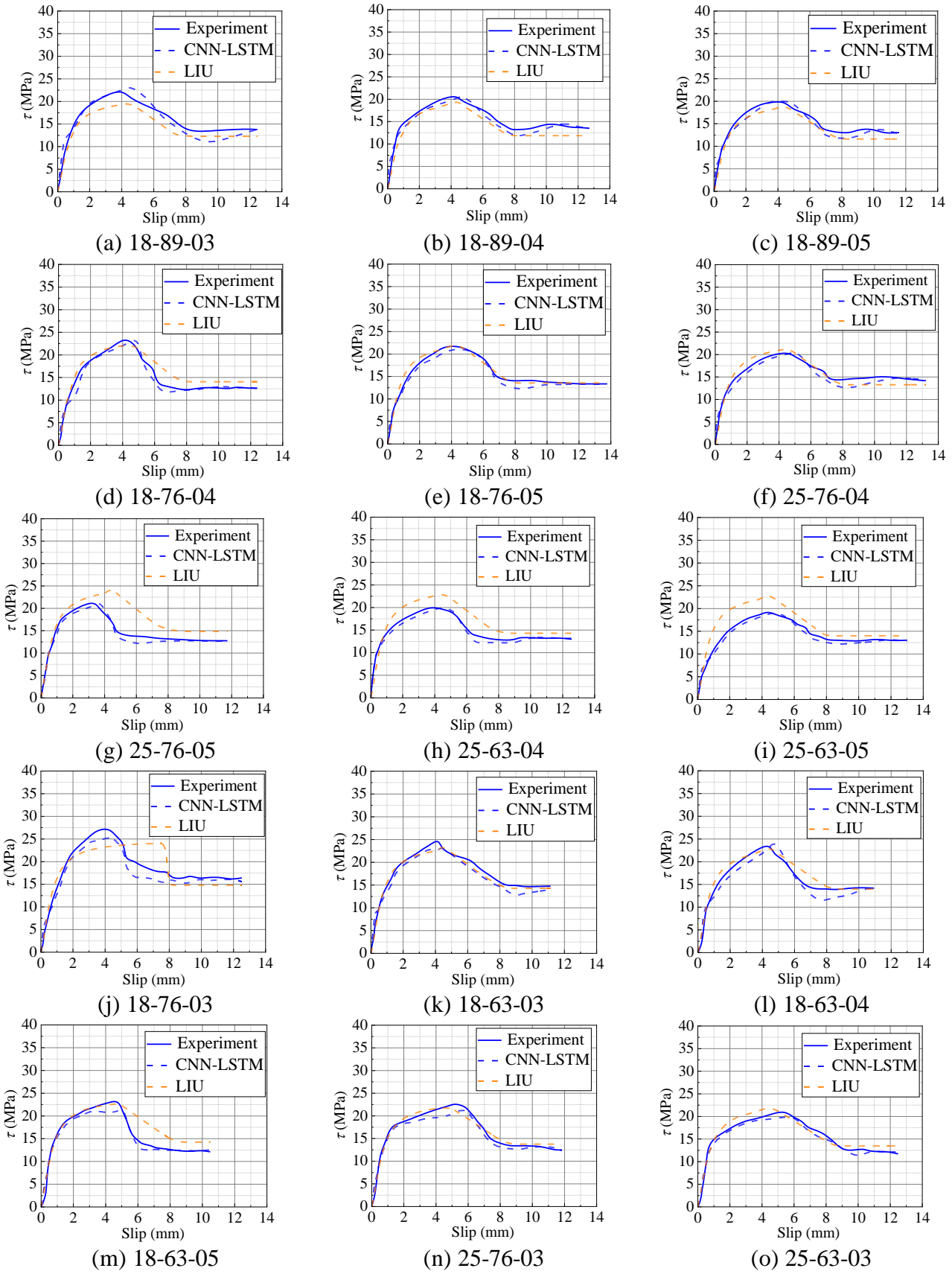


Figure 4. LIUs experimental prediction result.

Four indices—total energy consumption, maximum bond stress, failure modulus, and residual energy—were used to compare the differences between the bond-slip curves predicted by the empirical

model and the deep learning model, as shown in Figure 5. The ultimate bond stress, which is the maximum bond stress, is a crucial attribute representing the bond-bearing capacity of GBR system specimens. Total energy consumption refers to the energy consumed per unit area of the bond-slip curve from initial loading to residual stress (s_r), and is calculated using Equation 12. Residual energy refers to the energy consumed per unit area of the bond-slip curve from the ultimate stress (s_u) to the residual stress (s_r), and is calculated using Equation 13. Failure modulus is defined as the ratio of the ultimate bond stress to the ultimate slip, and it is used to evaluate the plastic deformation capability of GBR specimens. A higher modulus value indicates weaker plastic deformation ability and poorer ductility of the specimens. The calculation is shown in Equation 14.

$$W_{total} = \int_0^{s_r} \tau(s) ds \quad (11)$$

$$W_{residual} = \int_{s_u}^{s_r} \tau(s) ds \quad (12)$$

$$E_{failure} = \frac{\tau_u}{s_u} \quad (13)$$

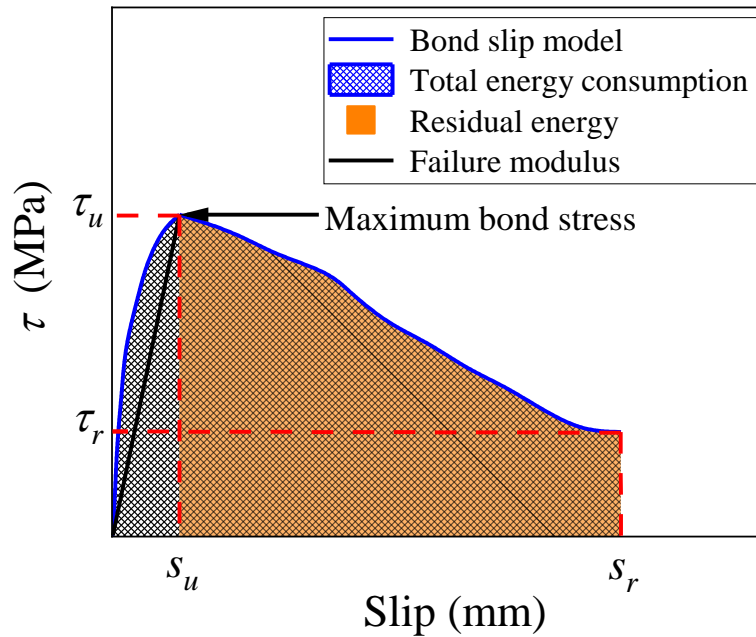


Figure 5. Adhesive slip evaluation index.

Figure 6 provides a clearer comparison of the prediction results between the CNN-LSTM model and the empirical model. In terms of total energy consumption, ultimate bond stress, and failure modulus, the CNN-LSTM results converge more closely around the red line compared to the empirical model. Regarding residual energy, the CNN-LSTM results are generally lower than the experimental results, whereas the empirical model shows relatively better accuracy. When combined with the observations from Figure 4, it can be concluded that this discrepancy arises because the ultimate slip prediction of the empirical model lags behind the test results. Residual energy is significantly influenced by the ultimate slip. When the descending portion of the empirical model curve is higher than that of the test curve, the energy loss

caused by the lag in ultimate slip can be compensated. Therefore, this does not imply that empirical models are superior in predictive accuracy.

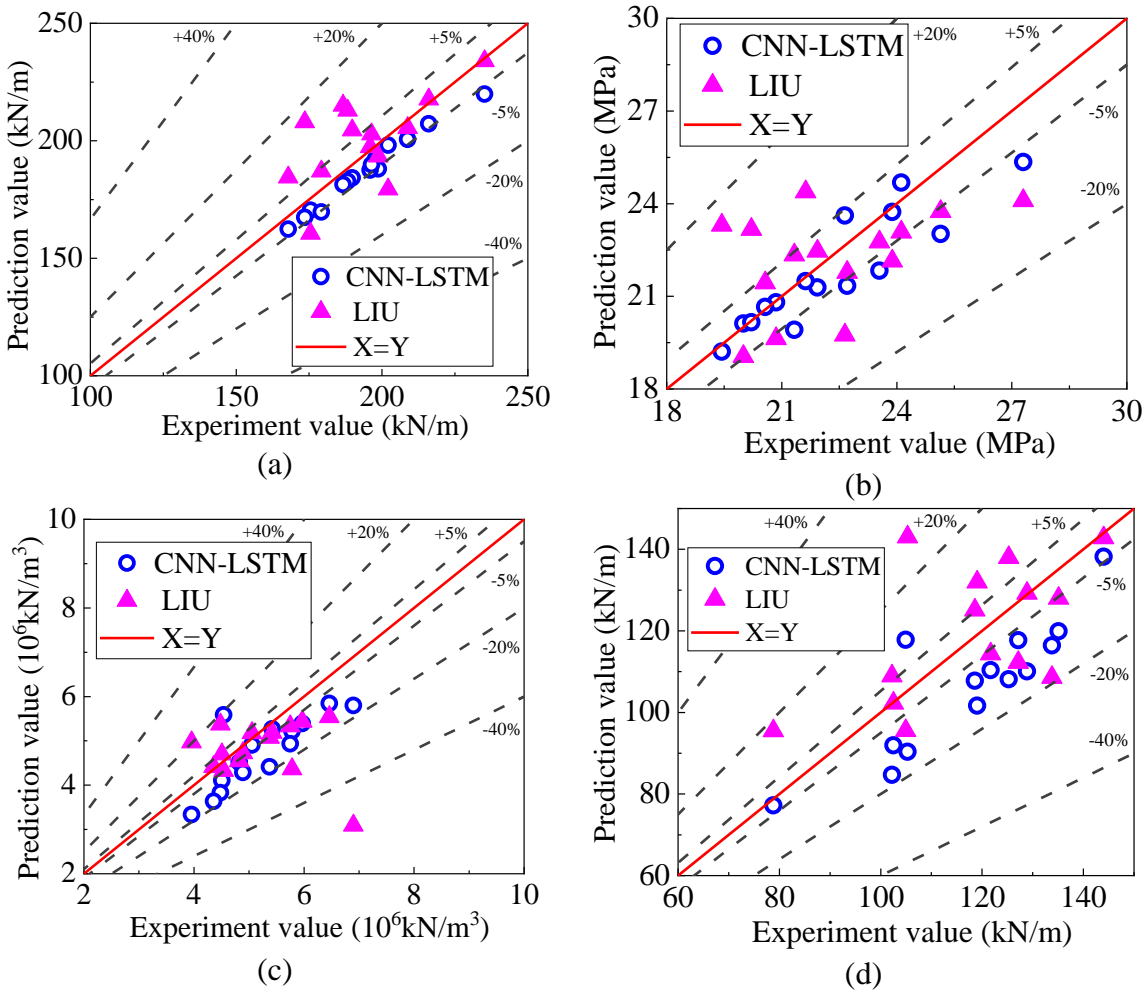


Figure 6. Adhesive slip evaluation index of LIU (a) Total energy consumption; (b) Maximum bond stress; (c) Component failure modulus; (d) Residual energy.

4.2. Generalization verification

To verify the generalization ability of the deep learning model, an additional 15 groups of specimens were designed for validation, as shown in Figure 1, with the loading scheme illustrated in Figure 2. The test scheme for each group is detailed in Table 4. The results for these specimens indicated adhesive slip failure, meaning the steel bar slipped away from the grout without being snap. The deep learning model, CNN-LSTM, was compared with the bond stress-slip empirical model, as shown in Figure 7. It is evident that the CNN-LSTM model prediction is closer to the experiment curve than those of the empirical model proposed by Liu. The predictions from Liu empirical model are conservative, with the ultimate bearing capacity predicted by the empirical model being significantly lower than the actual values. As indicated by Equations (3–7), Liu empirical model is closely related to the ratio of anchorage length to the diameter of the reinforcement, the ratio of the bellows aperture to the reinforcement, and the tensile strength of the grout.

Table 4. Test component parameter.

ID	f_c' (MPa)	f_g' (MPa)	l_r / d_r	d_b / d_r	D_r (mm)	f_u (MPa)	f_y (MPa)
I4003	39	3.11	3	2.5	117	633	454.7
I6403	39	3.11	3	4	117	633	454.7
I10003	39	3.11	3	6.25	117	633	454.7
I4005	39	3.11	5	2.5	117	633	454.7
I6405	39	3.11	5	4	117	633	454.7
I10005	39	3.11	5	6.25	117	633	454.7
I4007	39	3.11	7	2.5	117	633	454.7
I6407	39	3.11	7	4	117	633	454.7
I10007	39	3.11	7	6.25	117	633	454.7
II4003	39	5.165	3	2.5	117	633	454.7
II6403	39	5.165	3	4	117	633	454.7
II10003	39	5.165	3	6.25	117	633	454.7
II4005	39	5.165	5	2.5	117	633	454.7
II6405	39	5.165	5	4	117	633	454.7
II10005	39	5.165	5	6.25	117	633	454.7

The CNN-LSTM model was employed to predict the outcomes of Liu's experiment, and the results were compared with those obtained from the empirical model, as shown in Figure 7. The ultimate bond stress predicted by the empirical model is lower than the experimental values, whereas the predictions from the CNN-LSTM model are more consistent with the experimental trends. In Figure 7(a)–(l), the ultimate slip amount predicted by CNN-LSTM is closer to the experimental results than those predicted by the empirical model, with the predicted slip amount being lower than that calculated by the empirical model. However, in Figure 7(m)–(o), the ultimate slip amount predicted by CNN-LSTM is higher than that of the empirical model. This discrepancy occurs because, when the grouting strength is 5.165 MPa and the anchorage length is increased to 5 times the diameter of the steel bar, the steel bar in the GBR system can yield under tension, resulting in a bond-slip curve with a distinct yield extension curve. The empirical model results show a yield curve when the anchorage length is 3 times the diameter of the steel bar, which does not conform to the experimental findings. In Figure 7(a)–(l), compared to Figure 7(m)–(o), the ascending curve has a steeper slope, while the descending curve has a gentler slope. Conversely, the descending curve predicted by the empirical model contradicts this rule, whereas the CNN-LSTM predictions are more consistent with this behaviour. In summary, the CNN-LSTM model demonstrates superior predictive accuracy regarding the yield behaviour of the GBR system, as evidenced by its closer alignment with experimental results.

Comparing Figure 7(a)–(i) with Figure 7(j)–(o), the results indicate that the ultimate bond stress increases with the grouting strength. Both the empirical model and the CNN-LSTM model can predict this trend, but the empirical model yields lower results and adopts a more conservative design approach. When the grade of grouting material changes from Grade I to Grade II, the empirical model suggests an obvious yield rising curve. However, experimental results indicate that the anchorage length needs to increase to 5 times the diameter of the steel bar before an obvious yield curve appears. This discrepancy demonstrates that the empirical model is highly sensitive to individual component factors and exhibits poorer generalization performance compared to the CNN-LSTM deep learning model.

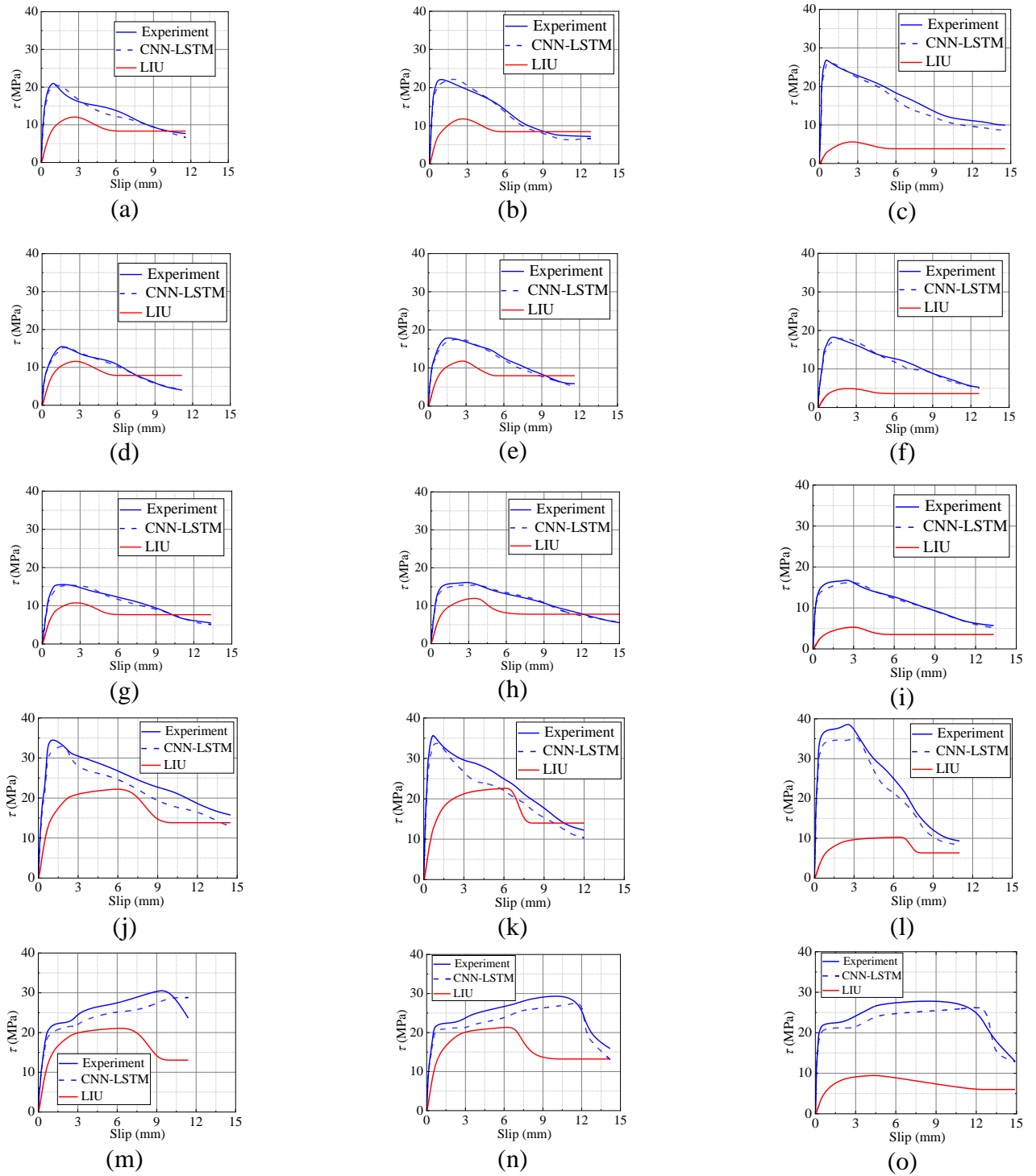


Figure 7. Experimental prediction result (a) I4003; (b) I6403; (c) I10003; (d) I4005; (e) I6405; (f) I10005; (g) I4007; (h) I6407; (i) I10007; (j) II4003; (k) II6403; (l) II10003; (m) II4005; (n) II6405; (o) II10005.

The four evaluation indices of the empirical model and the CNN-LSTM model are represented using scatter plots, as shown in Figure 8(a)–(b) demonstrates that the total energy consumption and ultimate bond stress predicted by the CNN-LSTM model are closer to the red line compared to the empirical model. Most of Liu model predictions are significantly lower than the experimental results, consistent with the conclusions drawn from Figure 7.

It is worth noting that the CNN-LSTM model does not perform as well in predicting the failure modulus and residual energy compared to total energy consumption and ultimate bond stress. This discrepancy arises because the failure modulus is merely a ratio, determined solely by the ultimate bond stress and ultimate slip. As the time series analysis network, CNN-LSTM predicts the next data point based on the previous time point data. While it can accurately predict the trend of the bond-slip curve to align with the test curve, it cannot precisely determine the occurrence time of the ultimate point. Figure 8(c) shows that the failure modulus predicted by CNN-LSTM is lower than the experimental value, the results are conservative, which is acceptable for engineering reliability analysis. In combination with Figure 7, it can be seen that the declining curve of CNN-LSTM is closer to the test value, and the difference is smaller than LIU's model. Given the good prediction results in Figure 8(b), it can be inferred that most of the ultimate slips predicted by CNN-LSTM are larger and lag behind the experimental results. In terms of residual energy, this property also depends on the timing of the ultimate point occurrence. Once this timing cannot be accurately determined, the prediction performance of the deep learning model for residual energy is worse than for the other two properties. Nevertheless, the first point of engineering design is usually conservative estimation, and the residual energy error can be covered by the safety factor. The second point is that the total energy consumption and the maximum bond stress are the core indicators of the design, and its high precision can ensure the safe modification of the structure. The total energy consumption and maximum bond stress predictions exhibited deviations of approximately 5% from experimental values, which has a tolerable influence on the structural design and prefabricated components. Overall, the CNN-LSTM model outperforms the empirical model.

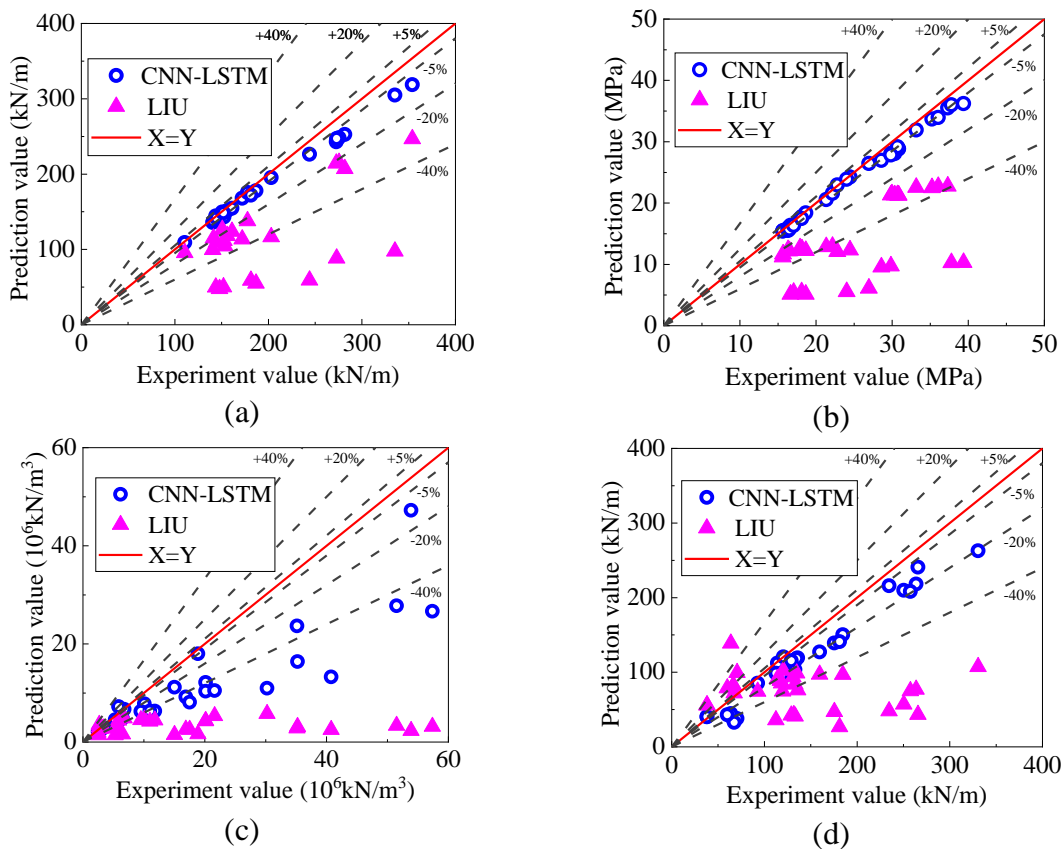


Figure 8. Adhesive slip evaluation index of experiment (a) Total energy consumption; (b) Maximum bond stress; (c) Component failure modulus; (d) Residual energy.

5. Discussion

5.1. Sensitivity analysis

A sensitivity analysis of the CNN-LSTM model was conducted to further investigate the seven important influencing parameters of GBR system specimens. This analysis aimed to determine the sensitivity of the factors listed in Table 3 to key evaluation indices of the bond stress-slip curve. The contribution and sensitivity of each factor to the bond anchoring performance of the GBR system were assessed. Feature sensitivity in deep learning is calculated using the mean influence value (MIV) method, as proposed by Dimopoulos [50]. The theoretical basis of this method is that feature sensitivity can be measured by the sum of squares of the product of the derivative and curvature of all samples for a given feature. This method can be implemented using MATLAB R2023b. The analysis results, after conversion, are shown in Figure 9. A result of less than 10% indicates that the factor has a very weak influence on the bond-slip index of the GBR system.

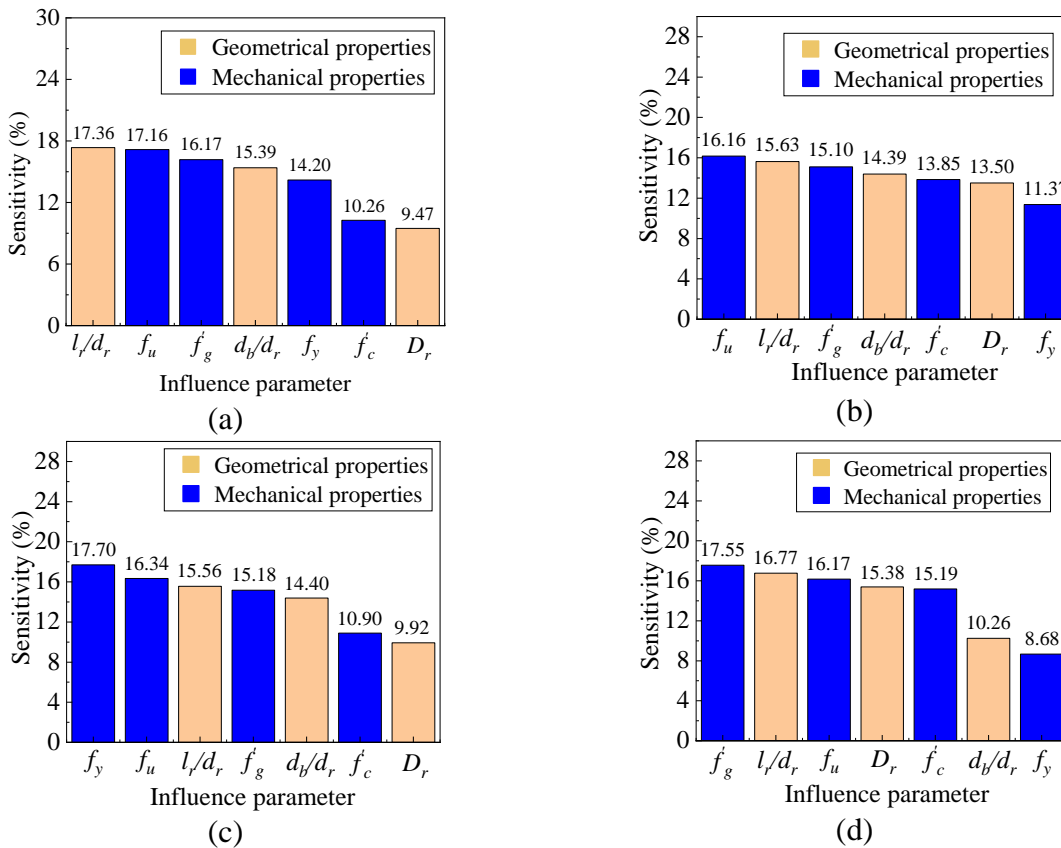


Figure 9. Sensitivity of the evaluation index (a) Total energy consumption; (b) Maximum bond stress; (c) Component failure modulus; (d) Residual energy.

The results indicate that for total energy consumption, maximum bond stress, and residual energy, the sensitivity of geometric and material factors to the GBR system is evenly distributed. However, the influence of material factors on the failure modulus is generally higher, suggesting that the overall stress behaviour and bearing capacity limit of the specimen are largely dependent on its material properties before failure occurs. This is because, prior to reaching the ultimate bearing capacity and subsequent failure, the bond-slip curve of the specimen undergoes cracking and yielding processes of the steel bar.

These processes are directly influenced by the yield strength of the steel bar and the strength of the grout material [51, 52]. Figure 9(a) shows that the parameters l_r / d_r , f_u , and f_g' contribute most significantly to total energy consumption. When these factors change, the total energy consumption is likely to change accordingly, as they have a substantial impact on the overall drawing process of the GBR system, with ridged reinforcement and grout being the primary forces. However, the influence of D_r is less than 10%, indicating a weak impact on the overall energy consumption of the GBR system. Figure 9(b) demonstrates that most factors can affect the maximum bond stress. Figure 9(c) illustrates the parameter sensitivity of the bond-slip curve before specimen failure, showing that the material properties of the rebar are crucial during early loading. Figure 9(d) indicates that after the failure of the GBR system, the descending curve of the bond-slip curve largely depends on the friction between the reinforcement bar and the grout. Both D_r and f_c' can provide the circumferential binding force of the specimen, thereby increasing the friction between the reinforcement bar and the inner surface of the grout. Consequently, the sensitivity of these two factors is greater than that of other indicators. Overall, the sensitivity of l_r / d_r , f_u , and f_g' to the GBR system is relatively high, while the sensitivity of D_r is relatively low.

5.2. Simplified model

Due to the inherent lack of interpretability in CNN-LSTM models, it is not feasible to provide a bond-slip model with explicit mathematical expressions. Therefore, a simplified bond-slip model is proposed to facilitate calculations. The bond-slip models used for theoretical analysis are often complex in form and rely on multiple assumptions [53–58], leading to uncertainties in actual construction and test results. Consequently, this study favours fitting the bond-slip model based on extensive experimental data. The hyperbolic model proposed by Haskett [59], which addresses the bond-slip relationship in reinforced concrete, is not directly applicable to GBR systems. Therefore, this study introduces a first-order polynomial combined with seven key features (f_c' , f_g' , l_r / d_r , d_b / d_r , D_r , f_u , f_y) to adjust the model parameters. The ultimate bond stress and ultimate bond slip predicted by CNN-LSTM are incorporated into this model. The formula for fitting the simplified model to the experimental data, based on the database in this study, is as follows:

$$\tau(s) = \begin{cases} \tau_u \times \left(\frac{s}{s_u}\right)^a, & 0 \leq s \leq s_u \\ \tau_u - a\tau_u \times \frac{s - s_u}{15 - s_u}, & s_u \leq s \leq 15 \end{cases} \quad (14)$$

$$a = (0.045 \times f_c' - 0.051 \times \left(\frac{l_r}{d_r}\right) - 0.0034 \times f_y + 0.0019 \times f_u - 0.022 \times \left(\frac{d_b}{d_r}\right) - 0.003 \times D_r - 0.09 \times f_g')$$

Figure 10 presents a comparison of the simplified bond-slip model calculated using CNN-LSTM and the empirical model based on 15 groups of samples in this study. The proposed simplified hyperbolic model aims to encapsulate the bond-slip characteristics of the GBR system, aligning well with the bond-slip trends observed in most test results. However, the simplified model depicted in Figure 10(a)–(l) does not accurately simulate the trend of the descending curve. It is more suitable for modeling the ascending curve of the bond-slip curve. The descending curve of the GBR system includes a residual curve, which cannot be adequately represented by a simple linear model. Nevertheless, the curve comparison in Figure 10 shows

that the curve deviation between the simplified model and the test value is within an acceptable range. The proposed simplified model serves as an efficient and reliable computational tool for structural engineers to rapidly assess the bond-slip behaviour and load-bearing capacity of Grouted Bellows Connect Rebar (GBR) systems in prefabricated building structural joints, thereby facilitating optimized joint design and enhancing structural reliability.

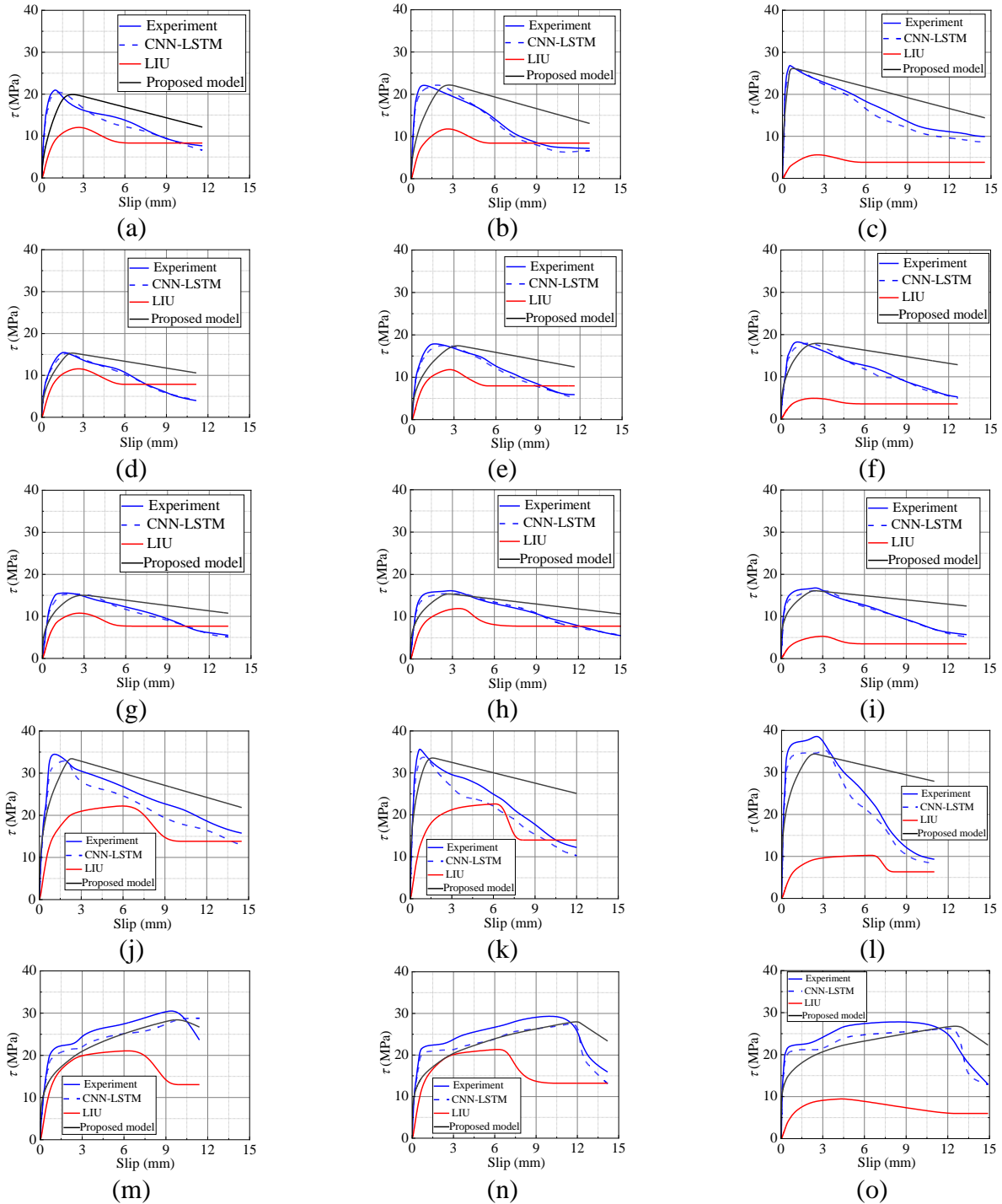


Figure 10. Simplified model comparison (a) I4003; (b) I6403; (c) I10003; (d) I4005; (e) I6405; (f) I10005; (g) I4007; (h) I6407; (i) I10007; (j) II4003; (k) II6403; (l) II1000.

5.3. Numerical simulation

To verify the feasibility of the simplified model (Equation 15) based on CNN-LSTM proposed in this study, and to ensure that the model can provide a reference for engineering design, finite element analysis of the GBR system was conducted using the numerical simulation software ABAQUS. The test model was replicated within the software, with concrete, bellows, rebar, and grout model being using the solid element C3D8R, and stirrups model was used the truss element T3D2. The interaction between the inner surface grid of the grout and the outer surface grid of the reinforcement was facilitated by an axial spring element [60], which possesses a single degree of freedom in the axial direction, this section is implemented by Python code, which is shown in the Appendix. This axial relationship reflects the local bond stress-slip interaction between the grout and reinforcement, defined according to the simplified model proposed in this study. The binding interaction between the inner surface of the concrete and the outer surface of the bellows, as well as between the inner surface of the bellows and the outer surface of the grout, was an also model. To ensure a proper fit for the spring unit between the steel bar and grout, a seed size of 5 is used for both components and the bellows during mesh division. However, as concrete is not the primary focus of this study, its seed size is set to 10 to enhance computational efficiency. Consequently, as detailed in the Appendix, ensure that the Set-100 for the rebar (Part1) and the Set-100 for the grout material (Part2) have an equal number of nodes, which are used to establish the Wire-Set node Set, thereby facilitating the effective creation of the spring unit. Given that the maximum displacement observed in the tests did not exceed 16 mm, the total displacement was distributed across the total time history using a displacement control model. The stress-strain relationship for concrete and grout was based on the concrete damage plasticity model [61].

The simulation was conducted on the 15 specimens listed in Table 4, yielding similar results. Due to space constraints, only the cloud map of the numerical simulation results for specimen I4003 is presented, as shown in Figure 11, which shows the cloud map of numerical simulation results. It can be seen that the stress distribution of grout is the largest near the free end (z direction in Figure 11), rather than at both ends of the grout, which is in line with the uneven distribution of bond stress studied by previous scholars [45,62]. As shown in Figure 12, the distribution function of adhesive anchorage position with adjacent surfaces indicates that the adhesive anchorage stiffness increases slowly before the anchorage depth of 0.8 times, which can be approximated by a quadratic curve, while the adhesive anchorage stiffness decreases sharply after the peak value, which can be approximated by an elliptic curve. This is also consistent with the simulated distribution of equivalent plastic stress of the grouting material of the test piece. As shown in Figure 11(a) of the reinforcement stress diagram, the loading end of the reinforcement is stressed most seriously during the drawing process, and the stress decreases with the increase of the anchoring depth, which will also result in the phenomenon of reinforcement pulling out, and the location of the pulling out is the location of the reinforcement outside the concrete, and the failure phenomenon is shown in Figure 11(c). The equivalent plastic strain diagram of the grout indicates the internal damage degree of the grout, and the most severely damaged area is concentrated at the loading end, while the grout at the outer edge of the loading end loses most of its bonding and anchoring force due to serious crushing, and the strain value is very small, so the blue part appears at the loading end. The failure phenomenon is shown in Figure 11(b).

Additionally, load-displacement curves under three typical working conditions were selected for comparative analysis, as illustrated in Figure 13. The numerical simulation results show good agreement with the test curves, with significant differences only appearing at the end of loading (when the slip is large). This indicates that the simplified bond-slip model proposed in this study is suitable for numerical simulation calculations, effectively capturing the bonding and sliding process between the steel bar and grout material within the bellows.

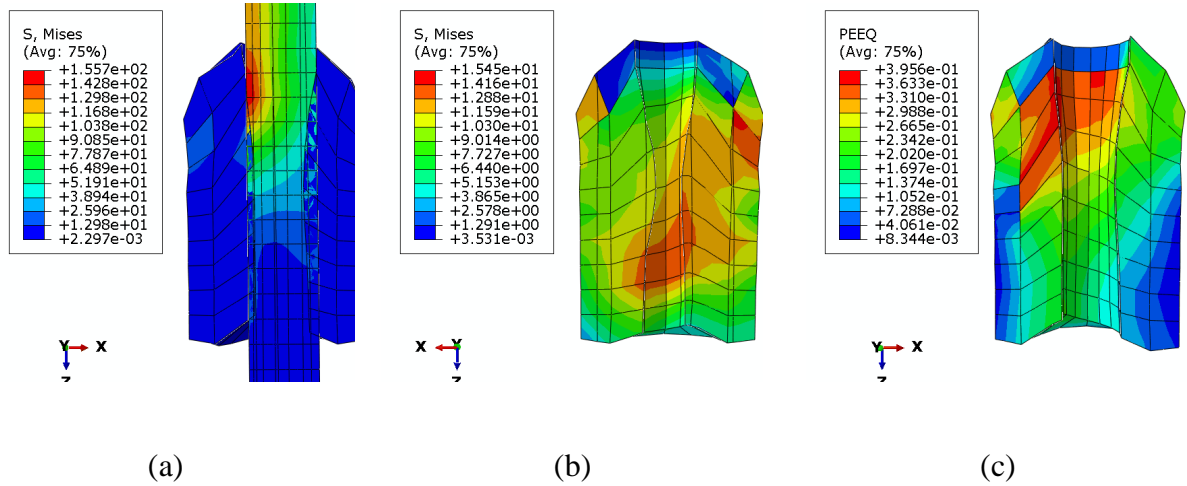


Figure 11. Numerical simulation result (a) I4003 stress envelope of steel bar; (b) I4003 stress envelope of grout; (c) I4003 plastic strain envelope of grout.

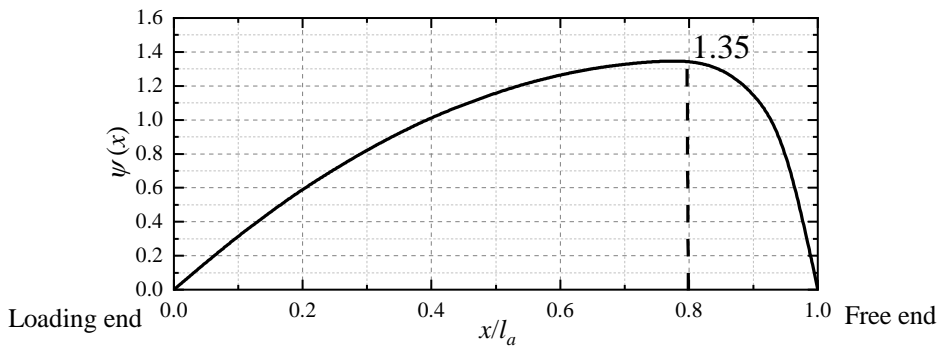


Figure 12. Numerical simulation result.

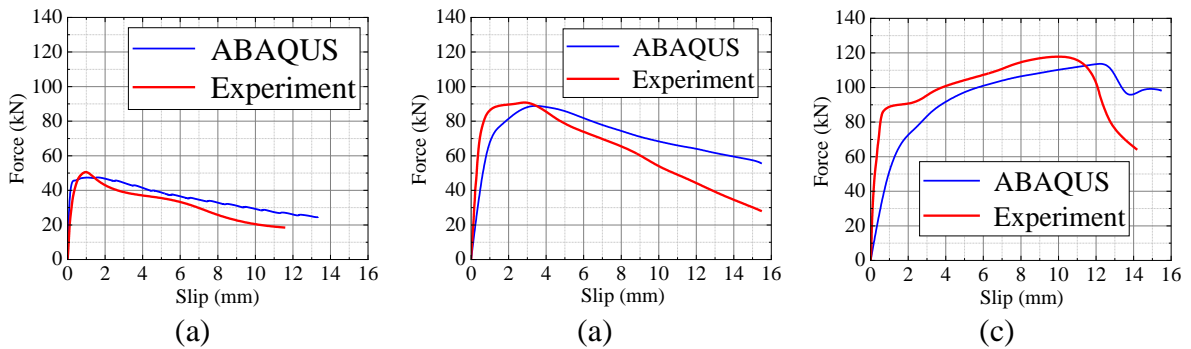


Figure 13. Load-slip curve comparison (a) I4003; (b) I6407; (c) II6405.

6. Conclusions

This study presents a CNN-LSTM model, a deep learning approach based on temporal neural networks, specifically designed to predict the bond-slip behaviour of GBR systems. A substantial database was compiled, comprising data from tests and designs adhering to actual engineering specifications for GBR systems. The CNN-LSTM model was trained using eight input features, encompassing the geometric and physical properties of the GBR system, such as grouting tensile strength, concrete strength, and steel yield strength. The anchoring performance of the CNN-LSTM model for GBR systems was evaluated by comparing it with traditional empirical models across various indices, including bond-slip curves, total energy dissipation, maximum bond stress, failure modulus, and residual energy dissipation. Furthermore, to assess the generalization ability of CNN-LSTM, the model was employed to predict pull-out tests of additional GBR system specimens and compared with empirical model predictions. A sensitivity analysis of the deep learning model was conducted to evaluate the influence of different input characteristics on the bond-slip model's indices. Finally, a simplified hyperbolic bond-slip model, which can be expressed mathematically, is proposed. This model emphasizes simplicity. The following conclusions are drawn:

- (2) To evaluate the generalization capability of the CNN-LSTM model, fifteen sets of GBR samples were fabricated. The predicted values from the CNN-LSTM model closely align with the test results. However, due to the temporal characteristics inherent in the CNN-LSTM approach, its predictive performance for failure modulus and residual energy is less accurate compared to its predictions for total energy consumption and maximum bond stress.
- (3) The predictive performance of both the empirical model and the CNN-LSTM model was evaluated based on four indices: total energy consumption, maximum bond stress, failure modulus, and residual energy. The results indicate that the CNN-LSTM model provides a more accurate assessment of bond-slip performance compared to the traditional empirical model.
- (4) The sensitivity of four bond-slip indices in the GBR system was analysed by evaluating key factors using the MIV method across 10 specimens. The analysis concluded that the ratio of reinforcement anchorage length to diameter, the ultimate strength of the reinforcement, and the strength of the grouting material are the most significant factors affecting the sensitivity of the GBR system. In contrast, the sensitivity associated with the shortest distance between the reinforcement and the edge of the specimen was found to be relatively weak.
- (5) Building upon the hyperbolic bond-slip model proposed by Haskett, a simplified bond-slip model has been developed utilizing the ultimate bond stress and slip values predicted by the CNN-LSTM model. Because the simplified model has the advantage of quick evaluation, the descending curve is fitted by linear function, so the deviation from the test value is large. However, this simplified model is suitable for numerical simulations and offers an efficient and practical approach for structural engineers to assess the anchorage performance of GBR systems.

Acknowledgements

Acknowledgments: Thanks to the support of the National Natural Science Foundation of China (Grant No. 52478504), Guangxi Key Research Program (No. Guike AB22036001, Guike AB21220046) and Hezhou Science and Technology Development Program (Hekeji 202229). Any views, findings or

conclusions expressed in this article do not necessarily represent the views of the National Natural Science Foundation of China Key Laboratory of Green Building and Energy Conservation.

Conflicts of interests

The authors declare no conflict of interest.

Authors' contribution

Xingshuo Yang: Conceptualization, Methodology, Software, Validation, Formal analysis, Investigation, Data curation, Writing – original draft, Writing – review & editing, Visualization. Min Zhang: Conceptualization, Resources, Writing – review & editing, Supervision. Yihu Chen: Resources, Supervision, Project administration, Funding acquisition. Jingchao Lin: Investigation, Data curation. Guangxin Xie: Investigation, Data curation. Yanwei Wang: Writing – review & editing, Project administration, Funding acquisition. All authors have read and agreed to the published version of the manuscript.

Appendix

```
#-*-coding:UTF-8-*-
session.journalOptions.setValues(replayGeometry=COORDINATE,recoverGeometry=COORDINATE)
from math import *
from abaqus import *
from abaqusConstants import *
from caeModules import *
from driverUtils import executeOnCaeStartup
executeOnCaeStartup()
Part1=str(str(getInput('Please enter the name of the fist target part'))+'-1')
Part2=str(str(getInput('Please enter the name of the second target part'))+'-1')
LENGTH = float(getInput('input the length of spring: '))
Springstiffness=float(getInput('input the Springstiffness of spring: '))
a = mdb.models['Model-1'].rootAssembly
n1 = a.instances[Part1].sets['Set-100'].nodes
list1 = []
num_1 = len(n1)
for i in range(num_1):
    list1.append((i,n1[i].coordinates[0],n1[i].coordinates[1],n1[i].coordinates[2]))
a = mdb.models['Model-1'].rootAssembly
n2 = a.instances[Part2].sets['Set-100'].nodes
list2 = []
```

```

num_2 = len(n2)
for j in range(num_2):
list2.append((j,n2[j].coordinates[0],n2[j].coordinates[1],n2[j].coordinates[2]))
list3 = []
for ii in range(num_1):
    for jj in range(num_2):
        if pow(((list1[ii][1]-list2[jj][1])**2+(list1[ii][2]-list2[jj][2])**2+(list1[ii][3]-
list2[jj][3])**2),0.5)<float(LENGTH):
            list3.append((list1[ii][0]+1,list2[jj][0]+1))
        else:
            continue
num_3=len(list3)
list4=[]
for iii in range(num_3):
    n1 = a.instances[Part1].sets['Set-100'].nodes
    n2 = a.instances[Part2].sets['Set-100'].nodes
    list4.append((n1[list3[iii][0]-1],n2[list3[iii][1]-1]))
a = mdb.models['Model-1'].rootAssembly
a.WirePolyLine(points=(list4), mergeType=IMPRINT,
    meshable=OFF)
a = mdb.models['Model-1'].rootAssembly
e1 = a.edges
edges1 = e1[0:num_3]
a.Set(edges=edges1, name='Wire-Set')

```

References

- [1] Jia J, Zhao N, Bai Y, Du X, Yang K, *et al.* Bond-slip model for rebar mounted to high-strength grouting material. *J. Build. Eng.* 2023, 74:106794.
- [2] Ling JH, Rahman ABA, Ibrahim IS, *Hamid ZA.* Behaviour of grouted pipe splice under incremental tensile load. *Constr. Build. Mater.* 2012, 33:90–98.
- [3] Zhang K, JIA J, Cheng S, Fan P, Pang W, *et al.* Seismic performance of emulative cast-in-place precast bridge columns state of the art review. *J. Beijing Univ. Technol.* 2022, 48(12):1248–1259.
- [4] Li YH, Yang ZP, Zhang HD, Luo YL, Zheng XH. Experimental study on anchoring performance of rebar-uhpc grout bellows. *Low Temp Archit Technol.* 2023, 45(04):129–132.
- [5] Steuck KP, Pang JBK, Eberhard MO, Stanton JF. Anchorage of large-diameter reinforcing bars grouted into ducts. 2007. Available: <https://utcdb.fiu.edu/wp-content/uploads/2021/09/UW-Rapid-Bridge-Construction-Nov-07.pdf> (accessed on 1 April 2025).
- [6] Zheng Y, Fan C, Ma J, Wang S. Review of research on bond-slip of reinforced concrete structures. *Constr. Build. Mater.* 2023, 385:131437.
- [7] Hayashi Y, Shimizu R, Nakatsuka T, Suzuki K. Bond stress-slip characteristic of reinforcing bars in grout-filled coupling steel sleeves. *J. Struct. Constr. Eng.* 1994, 59(462):131–139.
- [8] Yu Q, Xu XJ, You GS. Experimental study on bond behavior for ribbed steel bars and grout. *J. Wuhan Univ. Technol. Mater. Sci. Ed.* 2017, 49(12):91–101.
- [9] Hosseini SJA, Rahman ABA, Osman MH, Saim A, Adnan A. Bond behavior of spirally confined splice of deformed bars in grout. *Constr. Build. Mater.* 2015, 80:180–194.
- [10] Hosseini SJA, Rahman ABA. Effects of spiral confinement to the bond behavior of deformed reinforcement bars subjected to axial tension. *Eng. Struct.* 2016, 112:1–13.
- [11] Gu Q, Mei JH, Zhou K. Beam test of bond behavior of the steel bars in grouted hole of precast concrete. *J. Wuhan Univ. Technol. Mater. Sci. Ed.* 2018, 40(2):71–78.
- [12] Zhao JQ, Zhou L, Ding YG, Zhu RJ. Experiment on anchoring performance of spiral stirrup-corrugated pipe grout splicing. *J. Jilin Univ. (Eng. Technol. Ed.)*. 2024, 54(9):2484–2494.
- [13] Mao WH, Liu JP, Ding Y, Chen YF. Bond-slip constitutive model and numerical analysis for rebar embedded in steel-polyethylene hybrid fiber-reinforced cementitious composites. *Constr. Build. Mater.* 2021, 308:125092.
- [14] Vilanova I, Torres L, Baena M, Llorens M. Numerical simulation of bond-slip interface and tension stiffening in GFRP RC tensile elements. *Compos. Struct.* 2016, 153:504–513.
- [15] Goto Y. Cracks formed in concrete around deformed tension bars. *ACI J.* 1967, 64(11):711–721.
- [16] Liu JW. Anchorage performance of rebar-corrugated duct connection of precast bridge piers. Master's Thesis, Southeast University, 2021.
- [17] Zhu RJ. Experimental study on anchoring and lap performance of spiral stirrup-corrugated pipe grout anchor connection. Master's Thesis, Henan University of Technology, 2022.
- [18] Farouk AIB, Zhu J, Ding J, Haruna SI. Prediction and uncertainty quantification of ultimate bond strength between UHPC and reinforcing steel bar using a hybrid machine learning approach. *Constr. Build. Mater.* 2022, 345:128360.
- [19] Fan C, Zheng Y, Wang S, Ma J. Prediction of bond strength of reinforced concrete structures based on feature selection and GWO-SVR model. *Constr. Build. Mater.* 2023, 400:132602.

- [20] Su M, Zhong Q, Peng H, Li S. Selected machine learning approaches for predicting the interfacial bond strength between FRPs and concrete. *Constr. Build. Mater.* 2021, 270:121456.
- [21] Pishro AA, Zhang Z, Pishro MA, Xiong F, Zhang LL, *et al.* UHPC-PINN-parallel micro element system for the local bond stress–slip model subjected to monotonic loading. *Structures.* 2022, 46:570–597.
- [22] Yuan C, Xiong QS, Kong QZ. Multivariate time series deep neural network prediction of seismic hysteretic performance of reinforced concrete shear walls. *Eng. Mech.* 2024, 41(06):66–76.
- [23] Ni X, Xiong Q, Kong Q, Yuan C. Deep hysteretic net to predict hysteretic performance of RC columns against cyclic loading. *Eng. Struct.* 2022, 273:115103.
- [24] ACI Committee. *Building code requirements for structural concrete and commentary (ACI 318–08)*. American Concrete Institute, 2008.
- [25] Z J, X Y, H X, T X, L Y, *et al.* *Code for Design of Concrete Structures (GB 50010–2010)*, 2nd ed. China: China Architecture Industry Press, 2015. pp. 28–30.
- [26] Tazarv M, Saiidi MS. UHPC-filled duct connections for accelerated bridge construction of RC columns in high seismic zones. *Eng. Struct.* 2015, 99:413–422.
- [27] Teng ZM, Zhang HG. Experimental study of splitting bond failure and development length of reinforcing bars in reinforced concrete beams. *Chin. Civ. Eng. J.* 1989, (02):33–43.
- [28] Yerlici VA, Ozturan T. Factors affecting anchorage bond strength in high-performance concrete. *ACI Struct. J.* 2000, 97(3):499–507.
- [29] Chen J, Xiao Y, Yin Q. Bonding strength of rebar anchorage in embedded corrugated sleeve with high strength grout. *J. Build. Struct.* 2015, 36(07):140–147.
- [30] Rehm G. *Über die Grundlagen des Verbundes zwischen Stahl und Beton*. Berlin: Vertrieb durch Verlag von W. Ernst, 1961, pp. 39–40.
- [31] Lutz L, A, Gergely P. Mechanics of bond and slip of deformed bars in concrete. *ACI Int. Concr. Abstr. Portal J. Proc.* 1967, 64(11):711–721.
- [32] Broms BB. Technique for investigation of internal cracks in reinforced concrete members. *ACI Struct. J.* 1965, 62(1):35–44.
- [33] Xu YL. Experimental study of anchorage properties for deformed bars in concrete. Doctoral Thesis, Tsinghua University, 1990.
- [34] Brenes FJ, Wood SL, Kreger ME. Anchorage requirements for grouted vertical-duct connectors in precast bent cap systems: A summary. 2006, Available: https://ctr.utexas.edu/wp-content/uploads/pubs/0_4176_S.pdf (accessed on 1 April 2025).
- [35] Brenes FJ. Anchorage of grouted vertical duct connections for precast bent caps. Doctoral Thesis, University of Texas, 2005.
- [36] Guo JX. Study on cement-based grouting material and slurry-anchor connection performance for fabricated structure. Master’s Thesis, Chongqing University, 2022.
- [37] He Y. Experimental study on pull-out capacity of rebar anchored in embedded corrugated sleeve in the concrete-filled steel tubular. Master’s Thesis, Hunan University, 2020.
- [38] Pan NJ. Experimental study of anchoring performance of steel bars anchored into the embedded metal bellows. Master’s Thesis, Xiangtan University, 2018.
- [39] Liu YL. Study on mechanical properties of lap joint of embedded metal corrugated pipe pulp anchor. Master’s Thesis, Xiangtan University, 2019.

- [40] Chen J, Xiao Y, Yin Q. Bonding strength of rebar anchorage in embedded corrugated sleeve with high strength grout. *J. Build. Struct.* 2015, 36(07):140–147.
- [41] Guo JX, Hu SW, Qi H, Nie Y, TAO X, *et al.* Experimental study on anchorage property of rebar-metallicbellows slurry anchor connection considering grout age. *J. Civil Environ. Eng.* 2022, 46(02):108–116.
- [42] Zhu RJ. Experimental study on anchoring and lap performance of spiral stirrup-corrugated pipegrout anchor connection. Master's Thesis, Henan University of Technology, 2022.
- [43] Zhou Y, Ou YC, Lee GC. Bond-slip responses of stainless reinforcing bars in grouted ducts. *Eng. Struct.* 2017, 141:651–665.
- [44] Hu XZ. Experimental study on anchorage performance of grouting connection with rebar inserted corrugated ducts. *Railway Construction Technology*, 2020, (04):27–30;39.
- [45] Liu JW, Wang H, Sha B, Gao H, Xu YF, *et al.* Experimental study on the bond-slip constitutive relationship between rebar and corrugated duct confined grouting. *J. Harbin Eng. Univ.* 2021,42(06):818–824.
- [46] Zheng G, Chai WK, Katos V. A dynamic spatial–temporal deep learning framework for traffic speed prediction on large-scale road networks. *Expert Syst. Appl.* 2022, 195:116585.
- [47] Huang HJ, Zhang JR, Wu J, Song L. Testing study on tensile-shear resistance property of the bond of metal tube. *Sichuan Build. Sci.* 2007, (04):18–22,30.
- [48] Du YF, Zhang TY, Li H. Experimental study on bonding performance of corroded steel bars and grout in sleeve. *J. Hunan Univ. (Nat. Sci.)* 2022, 49(03):90–100.
- [49] Liu LL, Xiao JZ, Ding T, Zhang KJ. Test and simulation on bond behavior between sleeve grout and high strength steel rebar. *J. Tongji Univ. (Nat. Sci.)* 2021, 49(09):1275–1283.
- [50] Dimopoulos Y, Bourret P, Lek S. Use of some sensitivity criteria for choosing networks with good generalization ability. *Neural Process. Lett.* 1995, 2(6):1–4.
- [51] Qi J, Cheng Z, Ma ZJ, Wang J, Liu J, *et al.* Bond strength of reinforcing bars in ultra-high performance concrete: Experimental study and fiber-matrix discrete model. *Eng. Struct.* 2021, 248:113290.
- [52] Jiang DH, Shah SP, Andonian AT. Study of the transfer of tensile forces by bond. *ACI J.* 1984, 81(3):251–259.
- [53] Zhao WP, Xiao JZ. On bond-slip constitutive model between ribbed steel bars and concrete. *Eng. Mech.* 2011, 28(4):164–171.
- [54] Xu YL, Shen WD, Wang H. An experimental study of bond-anchorage properties of bars in concrete. *J. Build. Struct.* 1994, 15(5):26–36.
- [55] Gao XL. Test and simulation of bond performance between high-performance concrete and steel bars. Doctoral Thesis, Tongji University, 2003.
- [56] Xu YL. An experimental study of bond-anchorage properties of bars in concrete. Doctoral Thesis, Tsinghua University, 1990.
- [57] Jiang DH. Bond and slip between steel and concrete. *J. Tongji Univ.* 1984(4):8–17.
- [58] Gambarova PG, Rosati G. Bond and splitting in reinforced concrete: Test results on bar pull-out. *Mater. Struct.* 1996, 29(189):267–276.
- [59] Haskett M, Oehlers DJ, Ali MSM. Local and global bond characteristics of steel reinforcing bars. *Eng. Struct.* 2008, 30(2):376–383.

-
- [60] Hammaty Y, De Roeck G, Vandewalle L. Finite element modeling of reinforced concrete taking into consideration bond-slip. In *Proceedings of the 1991 ANSYS Conference*, Houston, USA, 1991, pp. 1–10.
- [61] Tian LB, Hou JG. Reasonable plastic damaged factor of concrete damaged plastic model of ABAQUS. *J. Hubei Univ. (Nat. Sci.)* 2015, 37(04):340–345;358.
- [62] Tassions TP, Yannopoulos PJ. Analytical study on reinforced concrete members under cyclic loading based on bond stress-slip relationships. *ACI J. Proc.* 1981, 78(3):206–216.